Correspondence and requests for materials should be addressed to Q.-H.Y. (qhyangcn@tju.edu.cn; yang.quanhong@mail.sz.tsinghua.edu.cn)

* These authors contributed equally to this work.

Towards ultrahigh volumetric capacitance: graphene derived highly dense but porous carbons for supercapacitors

Ying Tao[1]*, Xiaoying Xie[1]*, Wei Lv[1,2]*, Dai-Ming Tang[3], Debin Kong[1], Zhenghong Huang[4], Hirotomo Nishihara[5], Takafumi Ishii[5], Baohua Li[2], Dmitri Golberg[3], Feiyu Kang[2,4], Takashi Kyotani[5] & Quan-Hong Yang[1,2]

[1]School of Chemical Engineering and Technology, Tianjin University, Tianjin 300072, China, [2]Engineering Laboratory for Functionalized Carbon Materials, Graduate School at Shenzhen, Tsinghua University, Shenzhen 518055, China, [3]World Premier International (WPI) Center for Materials Nanoarchitectonics (MANA), National Institute for Materials Science (NIMS), Ibaraki 3050044, Japan, [4]Laboratory of Advanced Materials, School of Materials Science and Engineering, Tsinghua University, Beijing 100084, China, [5]Institute of Multidisciplinary Research for Advanced Materials, Tohoku University, Sendai 980-8577, Japan.

A small volumetric capacitance resulting from a low packing density is one of the major limitations for novel nanocarbons finding real applications in commercial electrochemical energy storage devices. Here we report a carbon with a density of 1.58 g cm^{-3}, 70% of the density of graphite, constructed of compactly interlinked graphene nanosheets, which is produced by an evaporation-induced drying of a graphene hydrogel. Such a carbon balances two seemingly incompatible characteristics: a porous microstructure and a high density, and therefore has a volumetric capacitance for electrochemical capacitors (ECs) up to 376 F cm^{-3}, which is the highest value so far reported for carbon materials in an aqueous electrolyte. More promising, the carbon is conductive and moldable, and thus could be used directly as a well-shaped electrode sheet for the assembly of a supercapacitor device free of any additives, resulting in device-level high energy density ECs.

E lectrochemical energy storage (EES) has attracted much attention in the past decades since it is believed to be a key solution in powering fast-developing mobile electronics, electric vehicles (EVs) and storing renewable energy for power grids[1,2]. The electrochemical capacitor (EC), also called supercapacitor or ultracapacitor, is one of the important EES devices. It stores charge with ions from solution at a charged electrode surface, and is characterized by a much higher speed to harvest or release energy than is the case for a secondary battery such as a lithium ion battery (LIB), although the energy density of ECs is normally far lower than that of LIBs[3,4]. In the last decade, many efforts have been made to improve the energy density of ECs by hybridizing carbon with non-carbon highly capacitive materials or optimizing the nanostructures of carbons[5–10], which are the most widely used electrode materials for ECs. Especially, the energy densities of the recently-emerging nanocarbons, such as carbon nanotubes or graphenes, as well as highly porous carbons prepared by the template technique, have been continuously upgraded to a very high level[11–13]. Regrettably, only gravimetric capacitive performance has been the focus of most of these cases and due to the low apparent densities (<0.8 g cm^{-3} in most cases), these nanomaterials normally possess relatively low volumetric capacitances[14–16]. More importantly, the low packing density of nanomaterials leads to large empty spaces in the electrode that are not effective for storing ions and may be flooded by the electrolyte, thereby increasing the weight of the device without adding capacitance[15]. Thus, devices fabricated with nanomaterials generally suffer from a low energy density based on their total weight, making it hard for them to be scaled up in real applications, such as the power supply of EVs. Moreover, with the mounting demands for compact and portable energy storage systems, increasing the utilization rate of the limited volume in an EES device is quite important from the application standpoint. To summarize, novel materials with high volumetric capacitance intended for a much improved device-level energy density, are urgently required for future practical applications of newly emerging novel carbon materials.

As one of the amazing examples of hexagonally bonded carbon, graphene is an attractive material for its unique electrical, mechanical, thermal, optical, chemical and electrochemical properties[17–21]. Various types of sp^2 carbon forms can be viewed as assemblies of graphene nanosheets which are organized in different ways, for example, wrapping-up into fullerenes, rolling into carbon nanotubes and stacking into graphites[21]. From this point of view, the capacitive performance of a carbon electrode for an EC device is dominated by the accessible surface of the graphene nanosheets that are the basic building blocks. Currently used electrode materials like activated carbons and novel nanocarbons are characterized by a large specific surface area that contributes to a high gravimetric capacitance, but the organization of perfect or defective graphene nanosheets in a low density structure results in limited volumetric capacitance. Of interest to chemists or materials scientists, graphene nanosheets may act as the real building blocks to realize bottom-up assembly of novel carbon nanostructures and even directly into three dimensional (3D) macroform materials with desired properties[22–34]. Typically, most of those graphene assemblies reported to date and seen as promising electrode materials[22–29] are formed from interlinked graphene nanosheets and show high specific surface area, excellent conductivity and open ion channels. However, like other nanocarbons, they usually have a low packing density with abundant empty space and hence are difficult to develop into materials with a high volumetric capacitance. Thus, how to achieve a highly compact graphene assembly but retain a high porosity is a challenging topic for materials scientists wishing to produce high volumetric capacitance carbon electrodes.

Here we report a novel close-grained graphene-based macroassembly that balances these two opposing characteristics. They have a porous microstructure (contributing to a specific surface area (SSA) of 370 m^2 g^{-1}) and large density (up to 1.58 g cm^{-3}), and are therefore potential ideal electrode materials with high volumetric capacitance. The obtained high density porous graphene macroform (abbreviated as HPGM) has a volumetric capacitance as high as ~376 F cm^{-3}, which is the highest observed in an aqueous electrolyte for carbon materials to the best of our knowledge (Supplementary Table S1). More promising, due to the easy shaping properties and acceptable conductivity, the excellent electrochemical properties of the obtained materials can, to the maximum extent, be used to fabricate devices since the shaped HPGM can be directly used as an electrode sheet and no additives are required. The maximum energy density of the fabricated devices with aqueous electrolytes is up to 13.1 Wh L^{-1} at a power density of 39.5 W L^{-1} and the power density is up to 5.9 kW L^{-1} at an energy density of 9.1 Wh L^{-1} (all based on a fabricated device).

Results

Self-assembly formation of high density but porous carbons starting from graphene oxide. Typically, the hydrothermal treatment of a graphene oxide (GO) suspension results in the formation of a 3D hydrogel-like assembly through an effective interlinkage of graphene nanosheets and freeze drying is normally used to fix the 3D network constructed of interlinked nanosheets and results in a spongy assembly (normally obtained porous graphene macroform, denoted as PGM). The upper part of Fig. 1a schematically illustrates the formation of PGM, that after freeze drying, retains the morphology of the parent hydrogel without visible shrinkage. PGM is thus characterized by abundant macropores and mesopores, and of course, some micropores, resulting in a very low apparent density (~0.02 g cm^{-3}). By comparison, the present study reports a unique graphene assembly, HPGM, with a highly compact but porous microstructure. As demonstrated in the lower part of Fig. 1a, evaporation-induced drying (herein vacuum drying at room temperature) is used for the removal of water from the hydrothermal hydrogel, which results in the formation of a very stiff rod-like material with an apparent volume shrinkage of about one eightieth the volume of the parent hydrogel. The novel graphene-derived macroform material, HPGM, is characterized by an apparent density as high as 1.58 g cm^{-3} (see details of the density measurement and determination in Methods Section and Supplementary Table S2),
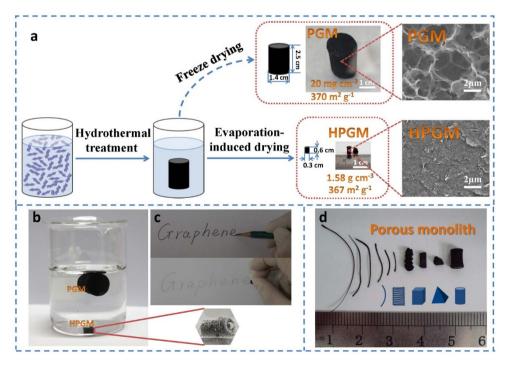

Figure 1 | Self-assembly formation of highly dense but porous graphene-based monolithic carbon (HPGM). (a) Schematic of the formation of graphene-based 3D porous macroforms with different drying process and the SEM images of the resultant PGM and HPGM. (b) PGM and HPGM in water, an enlarged view shows a rod-like HPGM with bubbling due to desorption of the adsorbed air. Note that material shown here is PGM with adsorbed water due to the hydrophilicity. (c) Rod-like HPGM (lower) for writing with a soft pencil (upper) as the reference. (d) Photograph of HPGM monoliths with different shapes but with similar SSA (300 ~ 500 m^2 g^{-1}).

which is ~70% of the theoretical density of graphite (2.2 g cm^{-3}). Of interest to us, HPGM is still characterized by a porous microstructure, indicated by a very simple experiment shown in the left panel of Fig. 1b, in which such a high density macroform generates bubbles in water due to the desorption of the absorbed air. The adsorption measurement gives a SSA of 367 m^2 g^{-1} and a pore volume of 0.16 cm^3 g^{-1}. Interestingly, this value is very close to that of PGM (370 m^2 g^{-1}) prepared from the same hydrogel, although both samples have entirely different volumes and apparent densities. Thus, the evaporation-induced drying of the graphene hydrogel produces a unique carbon not only with a high density but also a porous structure.

The self-assembly technique used allows HPGM to be moldable in two ways. On the one hand, we can obtain porous monoliths with desired shapes according to the mold used in the hydrothermal process. On the other hand, the hydrothermal product can be sliced or cut into any required shapes before further drying. Some typical examples for porous monolithic HPGMs with different shapes but similar SSA are presented in Fig. 1d and Supplementary Fig. S1.

Identification of highly compact but porous microstructure. Due to its highly compact structure, a rod of HPGM can be used for writing (the lower panel of Fig. 1c). In the X-ray diffraction (XRD) patterns (Fig. 2a), graphite and the soft pencil lead, which are similar in density to HPGM, are characterized by sharp (002) peaks (~26.5°) due to the layered structure, while such peaks are much broader and weaker for HPGM and annealed HPGM (denoted HPGM-800, annealed at 800°C). The results show that the arrangement of the graphene nanosheets in the graphene-derived porous carbons here is totally different from those in graphite or graphite products. It is likely that in HPGM highly wrinkled nanosheets are interlinked with each other to form a porous structure in a disordered but highly compact way.

Scanning electron microscopy (SEM) indicates the dense structure of HPGM (Fig. 1a and Fig. 2b). The typical cross-sectional SEM image shows a compact microstructure and no pore openings can be identified, indicating the totally different microstructure from spongy PGM in which large pores are clearly observed (Fig. 1a). In

other words, graphene nanosheets in HPGM are closely and neatly packed to form a very compact structure. High-resolution transmission electron microscopy (HRTEM) shows structural details at the nanoscale and intertwined nanosized pores constructed of curved graphene layers can be confirmed in HPGM under a microscope (Supplementary Fig. S2). As shown in Fig. 2c and 2d, with a post-annealing treatment at 800°C, HPGM-800 presents more distinct fringes for the curved nanosheets indicative of the contour of interconnected nanopores. Fig. 2c shows an overview for a region of such a novel carbon where totally interconnected pores, several nanometers in size (micropores and small mesopores), are observed and an unimpeded channel for ion transport is identified. This is naturally formed during the direct evaporation of the water trapped in the 3D pore network. In other words, nanopores in HPGM are formed after the 3D continuous porous structure of parent hydrogel. The shrinkage would not change the 3D interconnected porous character but only with a much smaller pore size, thereby the nanopores in HPGM being mutually connected. In Fig. 2d, many curved graphene layers and resulting cylindrical pores can be identified, and the pore walls normally consist of 2 ~ 4 layered nanosheets.

Since the present carbon is constructed of 3D interlinked nanosheets to produce intertwined nanopores, it is difficult to have an overall view in a single microscope image of a pore and accurate information about the pore size. More accurate information about the porous structure of HPGM is obtained by adsorption measurements[35]. The nitrogen cryoadsorption isotherms are shown in Fig. 3a and HPGM exhibits a Type I isotherm together with some characteristics for Type IV. That is, obvious micropore filling occurs at very low relative pressure and the adsorption process quickly reaches a well-defined plateau. A very small but identifiable hysteresis loop indicates the existence of a very limited amount of mesopores. Pore size distribution (PSD) curves (Fig. 3b) give more detailed information on the pore structure[13]. Except for a small peak around 2 nm, a single peak (centered at 1.1 nm) is observed in the micropore range (<2 nm in size) for HPGM, indicating that this carbon with cylindrical pores is a microporous carbon with a very limited amount of small size mesopores (slightly larger than 2 nm). That is, HPGM is
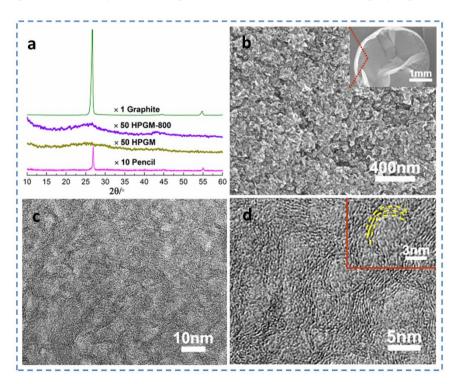

Figure 2 | Structure and morphological characterization of HPGM. (a) XRD patterns of graphite, soft pencil lead, HPGM and HPGM-800. (b) Cross sectional SEM images of HPGM, with the inset showing the cross-section of HPGM at low magnification. (c, d) TEM images of HPGM-800.
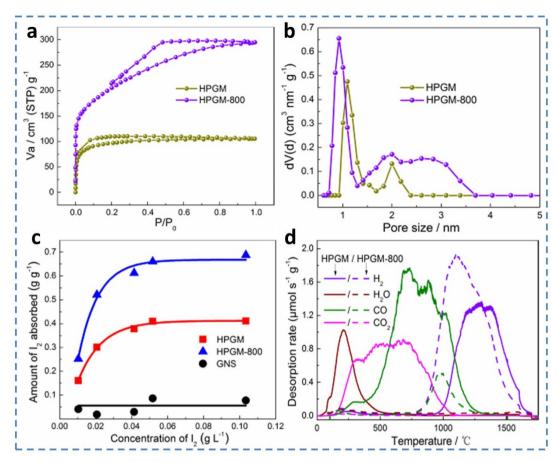
Figure 3 | Adsorption behaviors and surface nature of HPGM. (a) Nitrogen adsorption isotherms and (b) pore size distributions (DFT) of HPGM and HPGM-800. (c) Iodine adsorption isotherms of HPGM and the reference materials. (d) TPD spectra of HPGM and HPGM-800, including H_2, H_2O, CO, CO_2 evolution.

a microporous carbon (mostly with pores 1.1 nm in diameter) and free of large mesopores and macropores when used as a monolithic carbon. After annealing at 800°C (HPGM-800), the isotherm totally transforms into a composite isotherm combining Type I and Type IV. An increased adsorption amount at low pressure indicates an increase of the micropore volume while the appearance of a wide and more pronounced hysteresis loop is associated with more developed mesopores[36]. The analysis of the isotherm gives a SSA up to 720 m² g⁻¹ and a pore volume of 0.46 cm³ g⁻¹ for HPGM-800. The more developed pores result in a density decrease to 1.07 g cm⁻³, which is still higher than for most commercial activated carbons and reported novel porous carbons (0.3 ~ 0.8 g cm⁻³)[9,13,23–29,37] due to its monolithic form. The PSD curve (Fig. 3b) shows that HPGM-800 possesses pores that are mostly in the micropore (<2 nm) and mesopore ranges (2.0 ~ 3.7 nm). Compared with HPGM, HPGM-800 has a slightly smaller pore size in the micropore range possibly due to thermal shrinkage, and the appearance of pores from 1.3 to 3.7 nm may be due to the evolution of pores resulting from the removal of trapped water and bound oxygen. Microporosity in HPGM is further confirmed by iodine adsorption which is normally used for probing micropores[38] (Fig. 3c). HPGM-800 with more micropores, as expected, shows higher iodine adsorption than HPGM. In comparison, powdered graphene (GNS), which is totally free of micropores, shows a very small iodine adsorption although it possesses a larger SSA (450 m² g⁻¹) than does HPGM. Moreover, a relatively high adsorption rate for iodine indicates unimpeded channels in HPGM for adsorbates.

According to the X-ray photoelectron spectroscopy (XPS) analyses (Supplementary Fig. S3a), graphitic C (284.8 eV) is dominant in HPGM and the material contains far less oxygen (~16 at.%) than

the parent graphene oxide (30 ~ 40 at.%), indicating a partial reduction for HPGM in the hydrothermal process. Similar to the reduction process reported by Loh *et al.*, the supercritical water produced in the hydrothermal condition plays the role of reducing agent and offers an effective reduction approach for graphene oxide[39]. The rest of oxygen element in HPGM is mainly in the forms of C-O (286.2 eV) and C=O (287.6 eV) groups. After annealing at 800°C, the surface oxygen content decreases to ~4 at.% (Supplementary Fig. S3b and Table S3). Such a big decrease in oxygen content indicates that most oxygen-containing functional groups are removed and the resulting materials are reduced to a large extent. Temperature-programmed desorption (TPD) measurements indicate the thermal chemical desorption behavior of bound species on graphene nanosheets. In the case of HPGM, obvious CO_2 and CO peaks, which may respectively originate from carboxyl and lactone groups, and phenol and carbonyl groups[40], can be identified from the TPD spectra, revealing that there is still a considerable amount of surface oxygen groups left after the hydrothermal reduction. Significantly, an H_2O peak of HPGM centered at ~210°C suggests the existence of bound water trapped in the 3D porous network and results show that the trapped water is totally removed as the annealing temperature increases to 550°C (Fig. 4c). In contrast, after the annealing, for HPGM-800, there is only a small CO peak remaining at ~1000°C in addition to the total disappearance of the CO_2 peak. The results indicate that almost all surface groups and trapped water are removed except for a small amount of carbonyl groups. For HPGM-800, a very large hydrogen peak is observed and indicates the existence of a large amount of edge carbon atoms (saturated with hydrogen to form an open network). Such a hydrogen peak totally disappears above ~1550°C, and therefore, for HPGM-1600
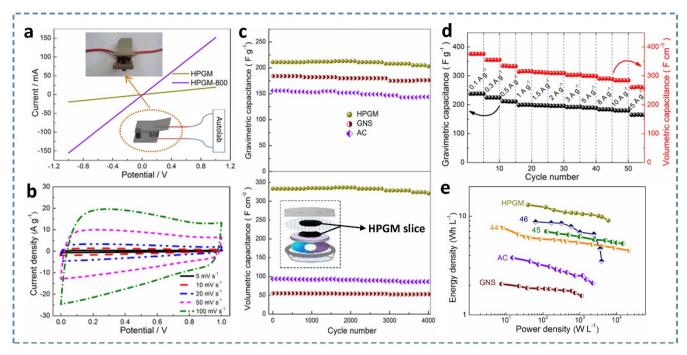
Figure 4 | Electrochemical performance of HPGM. (a) Room temperature I-V curves of HPGM and HPGM-800: the insets show the measurement apparatus for the conductivity test. (b) CV results of HPGM measured at scan rates of 5, 10, 20, 50, 100 mV s^{-1}. (c) Cycle performance of HPGM, GNS and AC at a current density of 0.5 A g^{-1}: the inset is a diagram of the two-electrode measurement device. (d) Rate performance of HPGM. (e) Volumetric Ragone plots comparing HPGM with AC, GNS and carbon materials reported in the reference number indicated.

(annealed at 1600°C), no visible hydrogen peak is observed (Supplementary Fig. S4a), which suggests a decrease in the number of edge carbons, indicative of a closed network. Such a difference in the hydrogen evolution peak for HPGM-800 and HPGM-1600 is consistent with the measured SSA values for the two carbons (the former with many edge carbons indicating an open network: 720 m^2 g^{-1}; the latter with fewer edge carbons indicating a closed network: 10 m^2 g^{-1} (Supplementary Fig. S4b)). Moreover, TEM images of HPGM-1600 (Supplementary Fig. S5) further demonstrate the changes of graphene network after annealing treatment.

Together with high density, shrinking during the vacuum drying increases the interlinking of graphene nanosheets, contributing to an acceptable conductivity of ~16 S m^{-1} for HPGM, which was directly measured as schematically shown in Fig. 4a. For comparison, spongy PGM has a lower conductivity of ~0.4 S m^{-1}, which is agreement with values reported elsewhere[22]. The annealing exerts a substantial effect on the microstructure of HPGM and a treatment temperature up to 1000°C results in both increases in SSA and conductivity. With a higher temperature treatment (>1000°C), the sample shows an apparent increase in conductivity but a substantial loss of SSA. HPGM-800 with higher SSA shows a good conductivity of 115 S m^{-1}, while HPGM-1600 shows a conductivity as high as 500 S m^{-1} but a very low SSA (~10 m^2 g^{-1}).

Compact structure and monolithic form needed to achieve an ultrahigh volumetric capacitive performance. Two-electrode supercapacitor cells (Supplementary Fig. S6) were constructed to assess the electrochemical performance in an aqueous system (6 M KOH). Note that due to its monolithic form and acceptable conductivity, sliced HPGM is directly used as an electrode in the assembly of supercapacitor devices without adding binders and conducting additives. PGM and HPGM show similar gravimetric capacitances in the aqueous system, the former with 235 F g^{-1} and the latter with 238 F g^{-1} at a current density of 0.1 A g^{-1}. In contrast, because of its low apparent density, PGM shows a very limited volumetric capacitance, even lower than 10 F cm^{-3}. In sharp contrast, with a very high

density (much reduced empty space), HPGM shows an ultrahigh volumetric capacitance, up to 376 F cm^{-3}, which, to the best of our knowledge (see the references in Supplementary Table S1 for comparison), is the highest value reported for carbon-based supercapacitor materials in an aqueous system. Even for a fabricated supercapacitor device, the energy density is very high due to the absence of any additives. Note that although thermal treatment results in an increase in both SSA (more developed porous structure) and conductivity, HPGM-800 possesses a much lower capacitance (about 80 F g^{-1} and 86 F cm^{-3}, Supplementary Fig. S7) than HPGM. Considering above results, it is likely that surface chemistry and trapped water other than specific surface area are the determining factors for the high capacitive performance of HPGM. In the case of HPGM-800, the substantial removal of oxygen-containing groups results in a big loss of pseudocapacitance as well as charged surface area which largely related to the wettability of graphene surfaces accessible to electrolyte ions[41,42]. The loss of trapped water hinders the formation of interconnected water passages, which reduces the full utilization of the graphene surface and brings the increased ion transfer resistance (Supplementary Fig. S8)[43]. Further investigations are ongoing to give more quantitative evidence for how various factors have influence on the capacitive performance of such a novel material.

For reference, the gravimetric and volumetric capacitances of powdered GNS and activated carbon (AC) as two typical commercial electrode materials for EDLCs are measured under the same conditions as for HPGM. Fig. 4b shows cyclic voltammetry (CV) profiles of HPGM at scan rates from 10 to 100 mV s^{-1}, and all curves show quasi-rectangular shapes indicating an ideal capacitive behavior. The gravimetric and volumetric capacitances were calculated based on galvanostatic charge/discharge curves (Supplementary Fig. S9) and the maximum volumetric capacitance of HPGM can reach 376 F cm^{-3} at 0.1 A g^{-1}. HPGM shows an excellent cyclability and, as shown in Fig. 4c, retains a specific capacitance up to 203 F g^{-1} and 321 F cm^{-3} at 0.5 A g^{-1} over 4000 cycles (the retention rate is over 96%). Remarkably, although totally free of conducting additives,
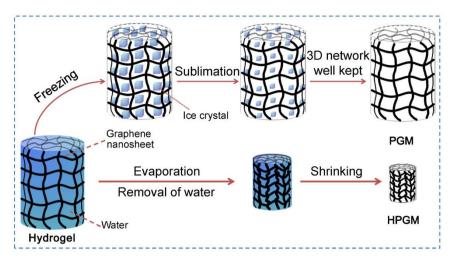
Figure 5 | The proposed formation process of PGM and HPGM starting from graphene hydrogel (Upper: PGM through freeze drying, lower: HPGM through evaporation-induced drying).

HPGM shows a very good rate capability while the capacitance was able to retain around 69% of the maximum at a high current of 15 A g^{-1} (Fig. 4d and Supplementary Fig. S10). The excellent rate performance can be attributed to the 3D porous network of interlinked graphene nanosheets which guarantee fast electron transfer and ion transport. On the one hand, with an acceptable conductivity, the 3D network of the HPGM provides an easily accessible conducting network. On the other hand, although HPGM only contains very small pores (mainly micropores together with very small mesopores), its interlinked 3D network structure together with trapped water in the pore network provides an unimpeded channel for fast ion transport. This is consistent with the previously reported results for fast ion transport in both interlinked micropores by Nishihara et al[13]. and water-trapped nanochannels by Li et al[43]. The Nyquist plot (Supplementary Fig. S11) shows very small equivalent series resistance (ESR) values corresponding to high conductivity and low internal resistance. As an important index for the ion diffusion process from electrolyte to the surface of the electrode material, the small Warburg resistance implies fast ion diffusion in the 3D network of HPGM. To better reveal the performance of HPGM, the Ragone plot of a HPGM based supercapacitor device is shown in Fig. 4e and Supplementary Fig. S12, with a comparison with AC, GNS and other carbon materials[44–46]. We can see that in the aqueous system, the maximum energy density of such a supercapacitor device is up to 13.1 Wh L^{-1} at a power density of 39.5 W L^{-1} and the power density is up to 5.9 kW L^{-1} at an energy density of 9.1 Wh L^{-1}. A much higher energy density can be achieved for a HPGM-based supercapacitor when an organic electrolyte is used (37.1 Wh L^{-1} at a power density of 98.8 W L^{-1}, as shown in Supplementary Table S4 and Fig. S13). These values are much higher than those of devices based on conventional carbon material, AC, and the newly emerging nanomaterials including GNS and carbon nanotubes for the same measurement conditions.

Discussion

The great difference in the morphology and microstructure of HPGM and PGM is ascribed to the different drying techniques, freeze drying or evaporation drying, used on the hydrothermal hydrogel and the key point is that in the different drying processes, the interactions between the water molecules being removed and the 3D graphene-based network are totally different. As schematically shown in Fig. 5, in the freeze drying case, when the parent hydrogel is frozen, phase separation can result in the rejection of graphene nanosheets from ice crystals (very weak interaction)[47,48], and in the finally formed PGM, the 3D network resulting from the

hydrothermal treatment is well retained during the subsequent sublimation process; while, in the evaporation-induced drying, the evaporation of water exerts a "pulling force" on the graphene layers and results in the shrinkage of the 3D network since there is strong interaction between water and graphene nanosheets. The robust but elastic 3D network constructed by interlinked and flexible graphene nanosheets shrinks but retains a porous structure inherited from the parent hydrogel during the removal of the evaporated water and the finally formed HPGM consists of curved and very compactly packed nanosheets with resulting interconnected small cylindrical pores, which is consistent with the TEM observations and excellent rate performance of HPGM in the electrochemical measurements. Together with microscopic observations as shown in Fig. 1a, the adsorption measurements (Supplementary Fig. S14) clearly indicate the microstructural differences between HPGM and PGM, the former exclusively with very small pores (micropores and small mesopores) but the latter containing a substantial amount of macropores and large mesopores in addition to the small pores. Compared with the freeze drying, the shrinkage in evaporation-induced drying induces a substantial loss of mesopores and macropores. Such shrinkage does not change the SSA to a large extent (HPGM: 367 m^2 g^{-1} and PGM: 370 m^2 g^{-1}; HPGM-800: 720 m^2 g^{-1} and PGM-800: 740 m^2 g^{-1}) since the SSA comes from the surface of graphene sheets and the shrinkage of pores only reduces the pore size and does not reduce the graphene surface area.

The uniqueness of its microstructure results in the excellent capacitive performance of HPGM, especially its ultrahigh volumetric capacitance. First, in spite of the much lower pore volume of HPGM than PGM, a similar accessible surface area and surface chemistry results in comparable gravimetric capacitances of the two materials with totally different microstructures. Second, a very dense microstructure, totally free of empty space, results in an ultrahigh materials-based volumetric capacitance. Third, a 3D porous network with trapped water, which can be totally removed above 550°C based on the TPD analysis, provides an intertwined canal-like network for fast ion transport especially in an aqueous system[43]. Evidently the removal of the trapped water from the 3D network results in an increased resistance of ion transport and a substantial decrease of the capacitance of HPGM-800. Fourth, the shrinking of the 3D network increases the interlinking of graphene nanosheets and results in an acceptable conductivity, which makes the additive-free monolithic HPGM an intrinsic electron conducting network. Last, but most important for a real device, the moldable monolithic form with fast ion transport and acceptable electron conductivity allows HPGM to be directly used for the assembly of an electrode

sheet and a final device without the need for any other binders or conducting additives, which contributes to a much improved device-level energy density.

In summary, we have developed a high density porous carbon resulting from the compact interlinking of 2 ~ 4 layered graphene nanosheets. The dense, porous and conductive microstructure of such a novel carbon contributes to a volumetric capacitance as high as 376 F cm^{-3}, the highest among those reported for an aqueous system thus far. Moreover, the fact that such a carbon is moldable and has an acceptable conductivity and unimpeded ion transport channels allows it to be directly used as an electrode sheet for a fabricated supercapacitor device, which results in device-level high energy density ECs. We believe that, together with our ongoing efforts to identify how monolayer graphene nanosheets organize in the most compact way to achieve a densely structured but more porous carbon, our results presented here suggest a simple but very effective way to produce compact and high performance EES devices for fast-developing EVs and multifunctional portable electronics.

Methods

Preparation of HPGM. Graphite oxide was prepared from graphite powder using a modified Hummers method as reported earlier[49]. A GO colloidal suspension (2 mg mL^{-1}) was prepared by ultrasonication of graphite oxide (170 mg) in water (85 mL) for 2 h, followed by mild centrifugation (3800 rpm for 20 min) to remove thick layers. Typically, the homogeneous GO colloidal suspension (85 mL) was placed in a 100 mL Teflon-lined autoclave, and treated by a hydrothermal process in a muffle furnace(150°C)for 6 h, resulting in a black cylindrical hydrogel. Such a hydrogel was washed, and then subjected to vacuum drying at room temperature, to produce HPGM. Additionally, HPGM-800 and HPGM-1600 were obtained by thermally treating HPGM for 3 h at 800°C and 1600°C respectively under Ar atmosphere.

For reference, PGM was produced from the same hydrogel using freeze drying and a following annealing of PGM at 800°C under Ar atmosphere yielded PGM-800.

Density measurement and determination. The densities (ρ) of the monoliths were obtained by the following three methods:

1) Densities were roughly calculated according to the mass of each sample and the physical dimensions due to very small porosity. Here, the averaged values of data are used.

2) Densities were determined by a balance (METTLER TOLEDO XS205) equipped with accessories for the density determination by the Archimedes principle.

3) Assuming the monoliths are free of macropores, ρ was calculated by the following equation:

$$\rho = \left(V_{total} + 1/\rho_T\right)^{-1} \qquad (1)$$

Where V$_{total}$ is the total pore volume estimated from the N$_2$ isotherm (77K), and ρ$_T$ is the true density (~2.11 g cm^{-3}) of the material determined by helium density measured on Belsorp-Max instrument (BEL Inc., Japan).

Note that the results for HPGM obtained from the three methods are almost in agreement due to the highly dense microstructure and monolithic form. For the convenience of comparison with other work, densities mentioned in the paper are the values calculated using method (3), i.e. based on the total pore volume and true density of material.

Characterization of the micro-morphology and structure. SEM and HRTEM observations were performed using a Hitachi S4800 (Hitachi, Japan) and a JEM 3100F (JEOL, Japan) respectively. XRD measurements were conducted at room temperature (Bruker D-8, Cu-Ka radiation, λ = 0.154056 nm).

Porous structure characterization. Nitrogen cryoadsorption (77 K) was measured by using a Belsorp-Max instrument (BEL Inc., Japan) and the sample was outgassed under vacuum at 200°C for 10 h before measurement. The SSA was obtained by Brunauer-Emmett-Teller (BET) analyses of the adsorption isotherm. Total pore volume (V$_{total}$) was calculated from the N$_2$ adsorption amount at P/P$_0$ = 0.99. The pore size distribution was calculated using density functional theory (DFT).

Iodine adsorption is measured as follows. An iodine stock solution of 0.103 g L^{-1} was diluted with deionized water to the required concentrations before use. Five samples, each weighing ~5 mg, were placed into 25 mL conical flasks. Iodine solutions (10 mL) with different concentrations were then added separately to each flask. The suspensions were shaken in the dark for 24 h at 30°C. After equilibrium, the remaining iodine in the supernatants was titrated with a 0.1 M sodium thiosulfate solution. The amount of iodine adsorbed expressed in (g g^{-1}) was calculated by the difference between the initial iodine solution and the iodine in the equilibrium solution.

Surface chemistry characterization. XPS was performed on a Thermo Scientific ESCALAB 250XI photoelectron spectrometer with Al Kα (1486.6 eV) as the X-ray source, two pass energies of 20 eV (survey scan) and 0.05 eV (high resolution scan) and a 650 μm beam size. The TPD profiles were obtained with an apparatus consisting of a reactor unit and a high vacuum detecting unit. The detailed method was described in ref. 50.

Electrical conductivity measurement. The electrical conductivity of the monoliths was measured by a two-probe method. I-V curves were recorded with an Eco Chemie Autolab 128N (Metrohm, Switzerland).

Electrochemical measurements in two-electrode system. Two slices of monoliths (each with a thickness of about 2 mm) were cut from the parent cylindrical hydrogel and subjected to vacuum drying at room temperature. We assembled two-electrode supercapacitors by sandwiching a non-conducting porous nonwoven cloth separator between the two dry solid-sheet samples and then immersing them in electrolyte (the dry slices were saturated with the electrolyte overnight beforehand). 6 M KOH aqueous solution and 1 M TEABF$_4$/AN were, respectively, used as aqueous and organic electrolytes for the assembly of supercapacitors. The assembly of the test cell using organic electrolyte was performed in a glove box filled with Ar. All the electrochemical tests were carried out at room temperature. Electrochemical impedance spectroscopy (EIS) was measured on the Eco Chemie Autolab 128N (Metrohm, Switzerland) equipped with a FRA2 frequency response analyzer module and Nova software, applying a perturbation voltage of 5 mV at open circuit potential in a frequency range from 10 mHz to 100 kHz. CV and galvanostatic charge-discharge measurements of the devices were performed on a CHI 660 electrochemical workstation (Chenhua, Shanghai, China) and LAND (Wuhan, China), respectively. The gravimetric and volumetric capacitances of one electrode were calculated from galvanostatic charge/discharge curves using the following equations:

$$C_S(F/g) = \frac{2I\Delta t}{m\Delta V} \qquad (2)$$

$$C_V\left(F/cm^3\right) = \rho \times C_S \qquad (3)$$

Where C$_S$ is the gravimetric capacitance of the single electrode, C$_V$ is the volumetric capacitance of the single electrode, I (amperes) is the discharge current, Δt (seconds) is the discharge time, m (g) is the mass of a single electrode, ΔV is the potential window during the discharge process after the IR drop, ρ is the density of the electrode which is here taken to be the density of the monoliths.

The specific capacitance of the supercapacitor cell was evaluated according to the following equation:

$$C_T(F/g) = \frac{C_S}{4} \qquad (4)$$

$$C_{V_T}\left(F/cm^3\right) = \rho \times C_T \qquad (5)$$

Where C$_S$ and C$_T$ are the specific capacitances of the electrode and the supercapacitor cell, respectively, C$_{V_T}$ is the volumetric capacitance of the supercapacitor cell, ρ is the density of the electrode.

The specific energy density and power density of the supercapacitor cell are defined as follows:

$$E(Wh/kg) = \frac{0.5C_T\Delta V^2}{3.6} \qquad (6)$$

$$E_V(Wh/L) = \rho \times E \qquad (7)$$

$$P(kW/kg) = \frac{E \times 3600}{\Delta t} \qquad (8)$$

$$P_V(kW/kg) = \rho \times P \qquad (9)$$

Where ΔV is the potential window during the discharge process after the IR drop, C$_T$ is the gravimetric capacitance of the supercapacitor cell, Δt (s) is the discharge time, ρ is the density of the electrode.

We used commercially available activated carbons (AC, Xinjiang, China) and graphene powder (GNS, prepared by the vacuum-promoted low-temperature exfoliation approach[49]) measured in a two-electrode system for comparison. In order to prepare electrode sheets, a mixture of the active material, poly(tetrafluoroethylene) (PTFE), and Super P with a weight ratio of 80 : 10 : 10 in an ethanol solution was ground together to form a homogeneous slurry. The slurry was spread into a film with a thickness of ~100 μm and then pressed on an Al foil current collector and dried overnight at 110°C under vacuum. The assembly of the test cell used the method given earlier.

1. Simon, P. & Gogotsi, Y. Materials for electrochemical capacitors. *Nature Mater.* 7, 845–854 (2008).

2. Liu, J. *et al.* Materials science and materials chemistry for large scale electrochemical energy storage: from transportation to electrical grid. *Adv. Funct. Mater.* **23**, 929–946 (2013).
3. Miller, J. R & Simon, P. Electrochemical capacitors for energy management. *Science* **321**, 651–652 (2008).
4. Winter, M. & Brodd, R. J. What are batteries, fuel cells, and supercapacitors? *Chem. Rev.* **104**, 4245–4269 (2004).
5. Jiang, H., Ma, J. & Li, C. Z. Mesoporous carbon incorporated metal oxide nanomaterials as supercapacitor electrodes. *Adv. Mater.* **24**, 4197–4202 (2012).
6. Zhi, M., Xiang, C., Li, J., Li, M. & Wu, N. Nanostructured carbon-metal oxide composite electrodes for supercapacitors: a review. *Nanoscale* **5**, 72–88 (2012).
7. Liang, Y., Wu, D. & Fu, R. Carbon microfibers with hierarchical porous structure from electrospun fiber-like natural biopolymer. *Sci. Rep.* **3**, 1119 (2013).
8. Arico, A. S., Bruce, P., Scrosati, B., Tarascon, J. M. & Van Schalkwijk, W. Nanostructured materials for advanced energy conversion and storage devices. *Nature Mater.* **4**, 366–377 (2005).
9. Nishihara, H. & Kyotani, T. Templated nanocarbons for energy storage. *Adv. Mater.* **24**, 4473–4498 (2012).
10. Xu, F. *et al.* Fast ion transport and high capacitance of polystyrene-based hierarchical porous carbon electrode material for supercapacitors. *J. Mater. Chem.* **21**, 1970–1976 (2011).
11. Liu, C., Yu, Z., Neff, D., Zhamu, A. & Jang, B. Z. Graphene-based supercapacitor with an ultrahigh energy density. *Nano Lett.* **10**, 4863–4868 (2010).
12. Zhu, Y. *et al.* Carbon-based supercapacitors produced by activation of graphene. *Science* **332**, 1537–1541 (2011).
13. Itoi, H., Nishihara, H., Kogure, T. & Kyotani, T. Three-dimensionally arrayed and mutually connected 1.2-nm nanopores for high-performance electric double layer capacitor. *J. Am. Chem. Soc.* **133**, 1165–1167 (2011).
14. Simon, P. & Gogotsi, Y. Capacitive energy storage in nanostructured carbon–electrolyte systems. *Acc. Chem. Res.* **46**, 1094–1103 (2012).
15. Gogotsi, Y. & Simon, P. True performance metrics in electrochemical energy storage. *Science* **334**, 917–918 (2011).
16. Frackowiak, E. & Beguin, F. Carbon materials for the electrochemical storage of energy in capacitors. *Carbon* **39**, 937–950 (2001).
17. Novoselov, K. S. *et al.* A roadmap for graphene. *Nature* **490**, 192–200 (2012).
18. Rao, C. N. R., Sood, A. K., Subrahmanyam, K. S. & Govindaraj, A. Graphene: the new two-dimensional nanomaterial. *Angew. Chem. Int. Ed.* **48**, 7752–7777 (2009).
19. Balandin, A. A. *et al.* Superior thermal conductivity of single-layer graphene. *Nano Lett.* **8**, 902–907 (2008).
20. Soldano, C., Mahmood, A. & Dujardin, E. Production, properties and potential of graphene. *Carbon* **48**, 2127–2150 (2010).
21. Geim, A. K. & Novoselov, K. S. The rise of graphene. *Nature Mater.* **6**, 183–191 (2007).
22. Xu, Y. X., Sheng, K. X., Li, C. & Shi, G. Q. Self-assembled graphene hydrogel via a one-step hydrothermal process. *ACS Nano* **4**, 4324–4330 (2010).
23. Chen, Z. *et al.* Three-dimensional flexible and conductive interconnected graphene networks grown by chemical vapour deposition. *Nature Mater.* **10**, 424–428 (2011).
24. Xu, Z., Zhang, Y., Li, P. & Gao, C. Strong, conductive, lightweight, neat graphene aerogel fibers with aligned pores. *ACS Nano* **6**, 7103–7113 (2012).
25. Wu, Z.-S. *et al.* Three-dimensional graphene-based macro- and mesoporous frameworks for high-performance electrochemical capacitive energy storage. *J. Am. Chem. Soc.* **134**, 19532–19535 (2012).
26. Tang, Z. H., Shen, S. L., Zhuang, J. & Wang, X. Noble-metal-promoted three-dimensional macroassembly of single-layered graphene oxide. *Angew. Chem. Int. Ed.* **49**, 4603–4607 (2010).
27. Zhang, X. *et al.* Mechanically strong and highly conductive graphene aerogel and its use as electrodes for electrochemical power sources. *J. Mater. Chem.* **21**, 6494–6497 (2011).
28. Worsley, M. A. *et al.* Mechanically robust 3D graphene macroassembly with high surface area. *Chem. Commun.* **48**, 8428–8430 (2012).
29. Zhao, Y. *et al.* A versatile, ultralight, nitrogen-doped graphene framework. *Angew. Chem. Int. Ed.* **51**, 11371–11375 (2012).
30. Lv, W. *et al.* One-pot self-assembly of three-dimensional graphene macroassemblies with porous core and layered shell. *J. Mater. Chem.* **21**, 12352–12357 (2011).
31. Cong, H.-P., Ren, X.-C., Wang, P. & Yu, S.-H. Macroscopic multifunctional graphene-based hydrogels and aerogels by a metal ion induced self-assembly process. *ACS Nano* **6**, 2693–2703 (2012).
32. Dong, Z. *et al.* Facile fabrication of light, flexible and multifunctional graphene fibers. *Adv. Mater.* **24**, 1856–1861 (2012).
33. Hu, H., Zhao, Z., Wan, W., Gogotsi, Y. & Qiu, J. Ultralight and highly compressible graphene aerogels. *Adv. Mater.* **25**, 2219–2223 (2013).
34. Bi, H. *et al.* Low temperature casting of graphene with high compressive strength. *Adv. Mater.* **24**, 5124–5129 (2012).
35. Storck, S., Bretinger, H. & Maier, W. F. Characterization of micro- and mesoporous solids by physisorption methods and pore-size analysis. *Appl. Catal., A* **174**, 137–146 (1998).
36. Tao, Y., Endo, M. & Kaneko, K. Hydrophilicity-controlled carbon aerogels with high mesoporosity. *J. Am. Chem. Soc.* **131**, 904–905 (2009).
37. Jorda-Beneyto, M., Lozano-Castello, D., Suarez-Garcia, F., Cazorla-Amoros, D. & Linares-Solano, A. Advanced activated carbon monoliths and activated carbons for hydrogen storage. *Micropor. Mesopor. Mat.* **112**, 235–242 (2008).
38. Abe, I. *et al.* Development of a high density carbonaceous adsorbent from compressed wood. *Carbon* **39**, 1485–1490 (2001).
39. Zhou, Y., Bao, Q., Tang, L. A. L., Zhong, Y. & Loh, K. P. Hydrothermal dehydration for the "green" reduction of exfoliated graphene oxide to graphene and demonstration of tunable optical limiting properties. *Chem. Mater.* **21**, 2950–2956 (2009).
40. Figueiredo, J. L., Pereira, M. F. R., Freitas, M. M. A. & Órfão, J. J. M. Modification of the surface chemistry of activated carbons. *Carbon* **37**, 1379–1389 (1999).
41. Fang, Y. *et al.* Renewing functionalized graphene as electrodes for high-performance supercapacitors. *Adv. Mater.* **24**, 6348–6355 (2012).
42. Zhao, B. *et al.* Supercapacitor performances of thermally reduced graphene oxide. *J. Power Sources* **198**, 423–427 (2012).
43. Yang, X. W., Zhu, J. W., Qiu, L. & Li, D. Bioinspired effective prevention of restacking in multilayered graphene films: towards the next generation of high-performance supercapacitors. *Adv. Mater.* **23**, 2833–2838 (2011).
44. Wang, D. W., Li, F., Liu, M., Lu, G. Q. & Cheng, H. M. 3D aperiodic hierarchical porous graphitic carbon material for high-rate electrochemical capacitive energy storage. *Angew. Chem. Int. Ed.* **47**, 373–376 (2008).
45. Chen, L.-F. *et al.* Synthesis of nitrogen-doped porous carbon nanofibers as an efficient electrode material for supercapacitors. *ACS Nano* **6**, 7092–7102 (2012).
46. Hu, J., Wang, H., Gao, Q. & Guo, H. Porous carbons prepared by using metal–organic framework as the precursor for supercapacitors. *Carbon* **48**, 3599–3606 (2010).
47. Qiu, L., Liu, J. Z., Chang, S. L., Wu, Y. & Li, D. Biomimetic superelastic graphene-based cellular monoliths. *Nat. Commun.* **3**, 1241–1247 (2012).
48. Li, W. L., Lu, K. & Walz, J. Y. Freeze casting of porous materials: review of critical factors in microstructure evolution. *Inter. Mater. Rev.* **57**, 37–60 (2012).
49. Lv, W. *et al.* Low-temperature exfoliated graphenes: vacuum-promoted exfoliation and electrochemical energy storage. *ACS Nano* **3**, 3730–3736 (2009).
50. Ishii, T., Orikasa, H. & Kyotani, T. in *Carbon* 2011, Extended Abstracts ID: 227 (Shanghai, China, 2011).

Acknowledgments

Author contributions

Q.-H.Y., Y.T. and W.L. conceived and designed the experiments. Y.T. carried out the materials synthesis and characterization, X.Y.X. and W.L. measured the electrochemical performance and analyzed the related data, D.-M.T. and D.G. performed TEM experiments and analysis. D.B.K. performed iodine adsorption, T.I. acquired TPD data, Z.H.H. and B.H.L. involved the analysis of adsorption data, H.N., T.K. and F.Y.K. gave important inputs in the interpretation of the formation mechanism. Q.-H.Y. and Y.T. were mainly responsible for preparing the manuscript with further inputs from other authors. All the authors discussed the results and contributed to the manuscript.

Additional information